

## PAPER

View Article Online  
View Journal

Cite this: DOI: 10.1039/d4ee00062e

## Engineering a zinc anode interphasial chemistry for acidic, alkaline and non-aqueous electrolytes†

Lin Ma,<sup>a</sup> Travis P. Pollard,<sup>a</sup> Marshall A. Schroeder,<sup>a</sup> Chao Luo,<sup>d</sup> Ye Zhang,<sup>e</sup> Glenn Pastel,<sup>a</sup> Longsheng Cao,<sup>f</sup> Jiaxun Zhang,<sup>f</sup> Vadim Shipitsyn,<sup>bc</sup> Yan Yao,<sup>e</sup> Chunsheng Wang,<sup>f</sup> Oleg Borodin<sup>\*a</sup> and Kang Xu<sup>§\*a</sup>

Reversibility and anode utilization remain key barriers to realizing practical, rechargeable Zn metal batteries. Herein, we report a heteroatomic molecule, 3,5-bis(trifluoromethyl)pyrazole (TFMP), capable of promoting a fluorinated and polymeric interphase in every class of zinc electrolyte (acidic, alkaline, non-aqueous). Significant improvements in performance are observed in TFMP-based electrolytes including coulombic efficiencies exceeding 99% and utilizations up to 80%. Notably, dendrite formation is effectively suppressed in all classes of electrolytes with the most impressive performance observed in weakly acidic aqueous media with selective entrainers. In full cells constructed with a thin (10- $\mu\text{m}$ ) Zn anode and an organic cathode, excellent performance is demonstrated with an exceptionally low n/p ratio (5.4) and high energy density (270 W h L<sup>-1</sup>, projected for 18 650 cell) in aqueous media. This work highlights that interphasial chemistries originating from additive-level electrolyte components can manifest major improvements without significantly altering the composition, cost, and key properties of traditional zinc electrolytes that were already optimized.

Received 5th January 2024,  
Accepted 26th February 2024

DOI: 10.1039/d4ee00062e

rsc.li/ees

## Broader context

Amid the global push for eco-friendly and efficient resource utilization, there's a compelling need for alternative battery systems that are able to supplement current Li-ion technologies. Rechargeable zinc metal batteries (RZMBs) present a compelling alternative, capitalizing on the significant advantages of zinc anode such as compatibility with aqueous electrolytes, and impressive volumetric and gravimetric capacity (5854 A h L<sup>-1</sup> and 820 mA h g<sup>-1</sup>). Nevertheless, the widespread adoption of RZMBs encounters challenges associated with electrochemical irreversibility and the suboptimal utilization of zinc metal. These challenges stem from dendritic growth during cycling and side reactions at the electrode-electrolyte interphase. Herein, we present an easily applicable strategy designed to notably improve the cycling performance of zinc metal anodes. This strategy demonstrates effectiveness across various solvent media selections, even at high areal capacities, ensuring 80% utilization of zinc anode. This proposed work hinges on introducing a heteroatomic molecule, specifically 3,5-bis(trifluoromethyl)pyrazole (TFMP). This addition serves to promote a fluorinated and polymeric interphase, thereby facilitating highly reversible Zn chemistry. This study provides novel insights into the deliberate control of zinc anode interphasial chemistries, offering exciting prospects for achieving practical RZMBs.

<sup>a</sup> Battery Sciences Branch, Energy Science Division, Army Research Directorate, DEVCOM Army Research Laboratory, Adelphi, MD 20783, USA.

E-mail: l.ma@charlotte.edu, marshall.a.schroeder.civ@army.mil, oleg.a.borodin.civ@army.mil, kang.xu@ses.ai

<sup>b</sup> Department of Mechanical Engineering and Engineering Science, University of North Carolina at Charlotte, NC 28220, USA

<sup>c</sup> Battery Complexity, Autonomous Vehicle and Electrification (BATT CAVE) Research Center, University of North Carolina at Charlotte, NC 28220, USA

<sup>d</sup> Department of Chemical, Environmental and Materials Engineering, University of Miami, Coral Gables, FL, 33146, USA

<sup>e</sup> Department of Electrical & Computer Engineering and Texas Center for Superconductivity at the University of Houston, University of Houston, Houston, TX 77204, USA

<sup>f</sup> Department of Chemical and Biomolecular Engineering, University of Maryland, College Park, MD, USA

† Electronic supplementary information (ESI) available. See DOI: <https://doi.org/10.1039/d4ee00062e>

‡ These authors contributed equally.

§ Current address: SolidEnergy Systems Corp., Woburn, MA 01801, USA.

## Main

Lithium-ion batteries (LIBs) are powering an electrification revolution with rapid adoption in electric vehicles, portable electronics, smart-grids and drones. However, given their intrinsic safety and supply chain concerns, the development of complementary battery chemistries is becoming increasingly important.<sup>1–3</sup> Rechargeable batteries based on a zinc metal anode offer a promising complement to LIBs due to key advantages such as compatibility with aqueous electrolytes, high volumetric and gravimetric capacity (5854 A h L<sup>-1</sup> and 820 mA h g<sup>-1</sup>),<sup>4,5</sup> and reduced reliance on critical elements like Co, Ni, and Li.<sup>6</sup> However, practical implementation of rechargeable Zn metal batteries (RZMBs) is still plagued by poor

Zn reversibility in plating/stripping and dendrite formation/growth.<sup>7–9</sup>

Compared to artificial interphase engineering,<sup>10,11</sup> electrolyte engineering is a proven and economical strategy for tuning both interfacial structures and interphasial chemistries, offering a drop-in approach toward enhancing Zn reversibility without compromising energy density or involving additional processes. The most common approaches are the addition or substitution of a primary component such as a new salt, additive, or co-solvent,<sup>12–17</sup> design of eutectic ionic liquids,<sup>18,19</sup> using polymer electrolytes,<sup>20,21</sup> or formulations intended to modify primary solvent structures.<sup>22,23</sup> Of these approaches, controlling the  $\text{Zn}^{2+}$  solvation environment has been recognized as the single-most effective method for improving reversibility in aqueous electrolytes. By modifying the  $\text{Zn}^{2+}$  solvation sheath to contain specific molecules or anions, these electrolytes form a stable interphase on the Zn metal anode. While these research directions have achieved notable progress, certain practical considerations impose limits on this strategy. For instance, the modification of  $\text{Zn}^{2+}$  solvation sheath in aqueous media often requires high concentrations of expensive salts<sup>24</sup> and co-solvents,<sup>25</sup> which will substantially increase the cell-level cost and reduce rate performance. Low salt solubility in organic solvents also restricts the compositional space for electrolyte design.<sup>26</sup> Most importantly, state-of-the-art electrolytes for Zn metal anodes still fail to enable sufficient reversibility under practical loading conditions (5 mA h cm<sup>−2</sup>, 10 mA cm<sup>−2</sup>, 80% utilization per cycle) as proposed for lithium metal anodes by Albertus *et al.*<sup>27,28</sup> This gap motivates the discovery of new electrolytes with engineered interphase chemistries.

In this work, we reveal how the addition of a fluorinated heteroatomic molecule, 3,5-bistrifluoromethyl pyrazole (TFMP), promotes reversible plating/stripping of Zn metal in all traditional classes of zinc electrolytes, including acidic, alkaline and non-aqueous systems. At only additive-levels (0.05 m) and with low Zn salt concentrations, TFMP enables dendrite-free Zn anodes with CEs above 99% under practical conditions (aqueous: 1.17 mA cm<sup>−2</sup>, 1.17 mA h cm<sup>−2</sup>, 20% utilization per cycle; non-aqueous: 9.36 mA cm<sup>−2</sup>, 4.68 mA h cm<sup>−2</sup>, 80% utilization per cycle). These performance improvements are ascribed to the polymerization of TFMP on the Zn metal surface, which forms a fluorinated polymer interphase that acts as a protective layer to suppress dendrite propagation and improve reversibility. We also find that this additive can act cooperatively with certain entrainers in aqueous media to further improve deposition uniformity and coulombic efficiency (CE). Due to TFMP's limited solubility in water, “entrainer” here signifies the addition of non-aqueous chemicals at levels below 1 m, serving the purpose of assisted-dissolution of TFMP and ensuring miscibility with aqueous solutions. Compared to other recently reported Zn electrolytes, additive-level amounts of TFMP can support RZMBs with high volumetric energy density and low n/p ratios with high-loading poly-(benzoquinonyl sulfide) (PBQS) and polyaniline (PANI) organic cathodes. This work demonstrates a unique and economical approach to electrolyte and interphase engineering for

high-performance RZMBs, without significantly altering electrolyte composition or using expensive salts at high concentrations.

## Zn metal anode reversibility

Using a galvanostatic protocol with a Cu|Zn (100 μm) cell configuration established in our previous work,<sup>26</sup> we initially examined the performance of electrolytes with TFMP in aqueous (1 m zinc bis(trifluoromethanesulfonyl)imide ( $\text{Zn}(\text{TFSI})_2$ ), Fig. 1(a) and Fig. S1, ESI†) and non-aqueous (0.5 m  $\text{Zn}(\text{TFSI})_2$  in acetonitrile (AN), Fig. 1(b)) media. Without compromising the electrochemical stability of aqueous electrolyte (Fig. S1, ESI†), the average CEs (calculated from eqn (1)) of these electrolytes are shown in Fig. 1(a) and (b) and represent a critical figure-of-merit for the reversibility of the  $\text{Zn}^{2+}/\text{Zn}$  chemistry. Remarkably, the addition of only 0.05 m TFMP in the water and AN-based electrolytes immensely improved the Zn CE up to 95.65% and 99.96%, respectively, as compared to the controls which fail due to parasitic reactions, as in previous work.<sup>26</sup> Interestingly, Zn CE was further improved to 97.39% in aqueous electrolyte with the addition of additive levels of TEP (Fig. 1(a) and Fig. S1, ESI†), suggesting a cooperative effect between TEP and TFMP. TFMP also enhanced Zn reversibility in other common aqueous electrolytes over a wide pH range (Fig. S1 and S2, ESI†), including mild acidic solutions (pH ~ 4–6) with  $\text{ZnSO}_4$ ,  $\text{Zn}(\text{OTf})_2$ , and alkaline solution (pH ~ 14) with potassium hydroxide (KOH); however, an additive-level entrainer (*e.g.* AN, MeOH) was required to dissolve TFMP in these aqueous media at similar concentrations (Fig. S3–S6, ESI†). Therefore, acidic, alkaline, and non-aqueous electrolytes with TFMP demonstrate much better reversibility in initial screening experiments with a Cu|Zn (100 μm) cell configuration.

Supporting a high per-cycle Zn utilization is a critical step toward improving the volumetric energy density of RZMBs.<sup>28</sup> Accordingly, we tested these modified baseline electrolytes with a more rigorous “reservoir-free” galvanostatic CE test protocol (Fig. S7 and S8, ESI†) in a Cu|Zn (10 μm) cell configuration. The 1 m  $\text{Zn}(\text{TFSI})_2$  + 1 m TEP + 0.05 m TFMP demonstrated stable cycling up to ~50 cycles with a high average CE (98.34%, calculated from eqn (2) for each cycle) and low Zn plating overpotential (~0.1 V) at current density of 1.17 mA cm<sup>−2</sup>, areal capacity of 1.17 mA h cm<sup>−2</sup>, and 20% Zn utilization per cycle (Fig. 1(d)), suggesting that interfacial side reactions as well as undesirable morphologies are effectively suppressed. In non-aqueous electrolytes, the addition of 0.05 m TFMP to AN enables extensive cycling (>600 cycles, 1200 h) with a low Zn plating overpotential (<0.2 V) and high average CE (99.91%, calculated from eqn (2) for each cycle) at 1.17 mA cm<sup>−2</sup>, 1.17 mA h cm<sup>−2</sup>, 20% Zn utilization per cycle (Fig. 1(c)). Even more surprisingly, stable cycling (>160 cycles) with an average CE of 99.9% (calculated from eqn (2) for each cycle) was also achieved at 9.36 mA cm<sup>−2</sup>, 4.68 mA h cm<sup>−2</sup>, and 80% Zn utilization per cycle (Fig. 1(e)). In comparison, the non-aqueous control cells failed early on due to the severity of the

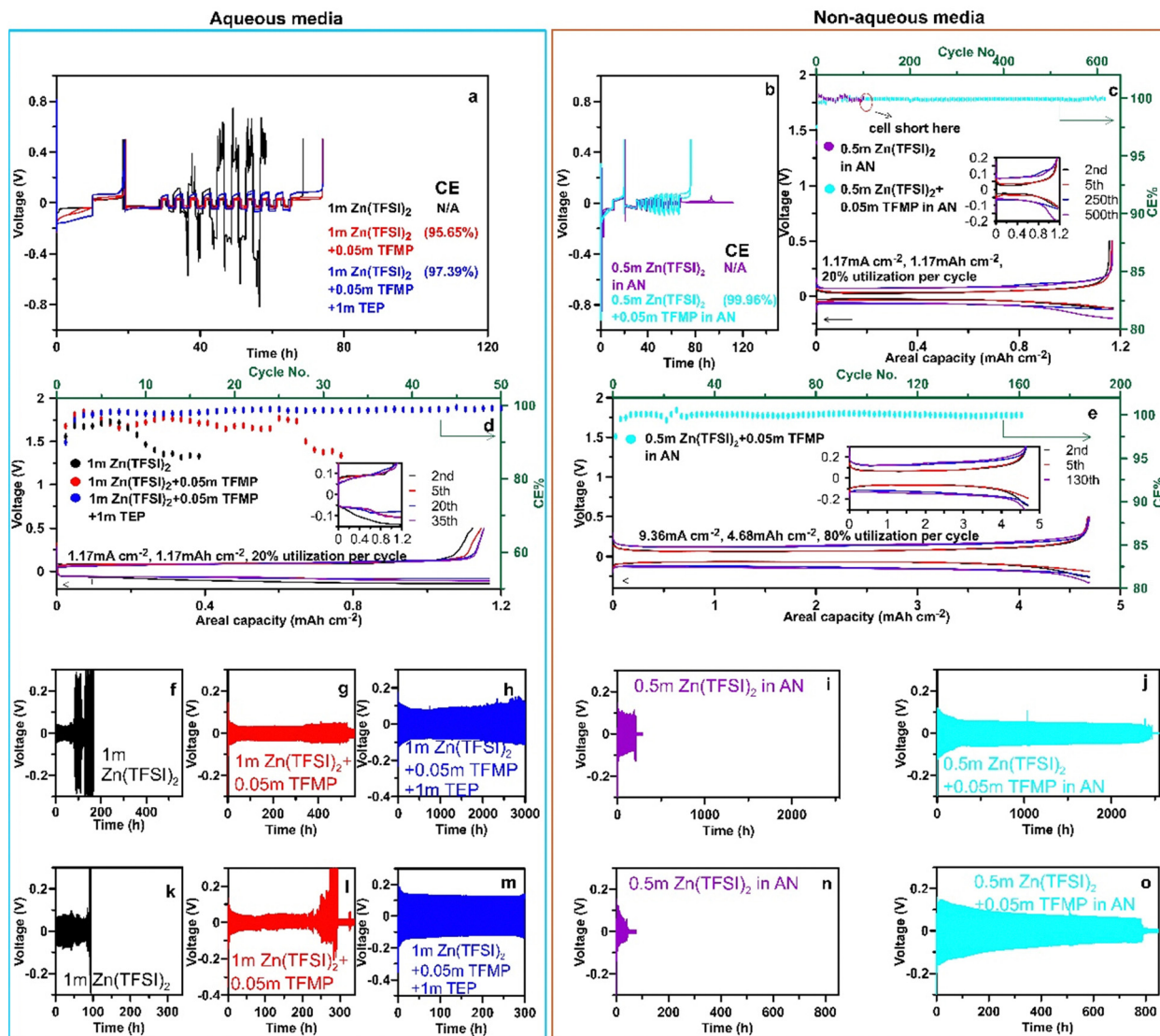


**Fig. 1** Zn metal anode reversibility in both aqueous and non-aqueous electrolytes. (a) and (b), Voltage profiles of Cu|Zn (100  $\mu\text{m}$ ) asymmetric cells during screening step with aqueous (a) or non-aqueous (b) electrolytes at room temperature. (c)–(e), Zn plating/stripping profiles and corresponding CE cycled using Cu|Zn(10  $\mu\text{m}$ ) cell setup at room temperature in aqueous (d) or non-aqueous (c) and (e) electrolytes with different testing conditions:  $1.17\text{ mA cm}^{-2}$ ,  $1.17\text{ mA h cm}^{-2}$  per cycle (c) and (d);  $9.36\text{ mA cm}^{-2}$ ,  $4.68\text{ mA h cm}^{-2}$  per cycle (e). (f)–(o), Voltage profiles of Zn|Zn (100  $\mu\text{m}$ ) symmetric cells during long-term cycling in aqueous (f)–(h), (k)–(m) or non-aqueous (i), (j), (n)–(o) electrolytes with different testing conditions:  $1\text{ mA cm}^{-2}$ ,  $1\text{ mA h cm}^{-2}$  per cycle (f)–(j);  $2.5\text{ mA cm}^{-2}$ ,  $2.5\text{ mA h cm}^{-2}$  per cycle (k)–(o) at room temperature.

CE testing protocol (Fig. S8, ESI<sup>†</sup>). The TFMP electrolytes enable cycling rigorous “reservoir-free” configurations with high utilization and CE with additive-level inclusions of TFMP and TEP entrainer, with TEP entrainer increasing overpotential and presenting a potential trade-off between improvement of CE and overpotential.

To gauge the propensity for dendrite formation and excessive polarization, these electrolytes were also tested in a Zn|Zn (100  $\mu\text{m}$ ) symmetric cell configuration under two aggressive galvanostatic conditions:  $1\text{ mA cm}^{-2}$ ,  $1\text{ mA h cm}^{-2}$  per cycle and  $2.5\text{ mA cm}^{-2}$ ,  $2.5\text{ mA h cm}^{-2}$  per cycle for extended durations. In aqueous media, control cells with  $1\text{ M Zn(TFSI)}_2$  fail quickly ( $<100\text{ h}$ , Fig. 1(f) and (k)) due to excessive polarization. In comparison, the addition of  $0.05\text{ M TFMP}$  (Fig. 1(g), (l))

or Fig. 1(m) TEP +  $0.05\text{ M TFMP}$  (Fig. 1(h) and (m)) extends the lifetime substantially to  $\sim 500\text{ h}$  (Fig. 1(g)),  $\sim 210\text{ h}$  (Fig. 1(l)),  $\sim 3000\text{ h}$  (Fig. 1(h)), and  $\sim 300\text{ h}$  (Fig. 1(m)), respectively. In non-aqueous media, the addition of  $0.05\text{ M TFMP}$  in AN also enhances cycle lifetime by suppressing Zn dendrite formation for  $\sim 2500\text{ h}$  at  $1\text{ mA cm}^{-2}$ ,  $1\text{ mA h cm}^{-2}$  (Fig. 1(j)) and  $\sim 800\text{ h}$  at  $2.5\text{ mA cm}^{-2}$ ,  $2.5\text{ mA h cm}^{-2}$  (Fig. 1(o)). In contrast, control cells suffer from “soft-short” circuits within a much shorter term ( $<200\text{ h}$ ) under both loads (Fig. 1(i) and (n)). According to Li *et al.*,<sup>29</sup> “soft-short” refers to the minor localized electrical link between two electrodes that enables the simultaneous occurrence of direct electron transfer and interfacial reaction. Unlike the common definition of “hard-short”, the leakage of electron is not persistent because the pathway



established between the electrodes subject to transient fluctuations. Therefore, the interphase enabled by additive-levels of TFMP not only improves CE and utilization, but also helps maintain low dendrite susceptibility and overpotentials.

## Postmortem analysis

Analyses using X-ray photoelectron spectroscopy (XPS) depth profiles, focused ion beam-scanning electron microscope (FIB-SEM), transmission electron microscopy (TEM), time of flight secondary ion mass spectrometry (ToF-SIMS) and density functional theory (DFT) calculations reveal the effect of TFMP on Zn electrode morphology and solid electrolyte interphase (SEI) evolution during cycling in both aqueous and non-aqueous electrolytes. Zn samples were recovered from a Zn|Zn (100  $\mu\text{m}$ )

symmetric cell configuration after 10 h and 200 h cycling at 0.5  $\text{mA cm}^{-2}$  and 0.5  $\text{mA h cm}^{-2}$  at room temperature, respectively. Compared to a pristine Zn electrode (Fig. S9, ESI<sup>†</sup>), the surface morphology of the recovered Zn is no longer flat, with increased surface area even at a very early stage of cycling (10 h, Fig. 2(a), (f) and Fig. S10, ESI<sup>†</sup>) in aqueous media, most likely due to competition between hydrogen evolution in the mildly acidic aqueous electrolyte (Fig. S2, ESI<sup>†</sup>) and  $\text{Zn}^{2+}/\text{Zn}$  redox on the electrode. The presence of  $\text{ZnF}_2$  signatures ( $\sim 685$  eV) in the F1s spectra (Fig. S10, ESI<sup>†</sup>) for the aqueous 1 m  $\text{Zn}(\text{TFSI})_2$  control sample, suggesting decomposition of the  $\text{TFSI}^-$  anion<sup>30</sup> is counterintuitive because some studies have shown that the  $\text{TFSI}^-$  anion undergoes a coupled reduction and defluorination at lower potentials.<sup>18,31</sup>  $\text{ZnF}_2$  could, however, form either as a result of a high barrier, slow reaction between  $\text{TFSI}^-$  and  $\text{OH}^-$ ,<sup>32</sup> or during reduction of the  $\text{TFSI}^-$  anion on

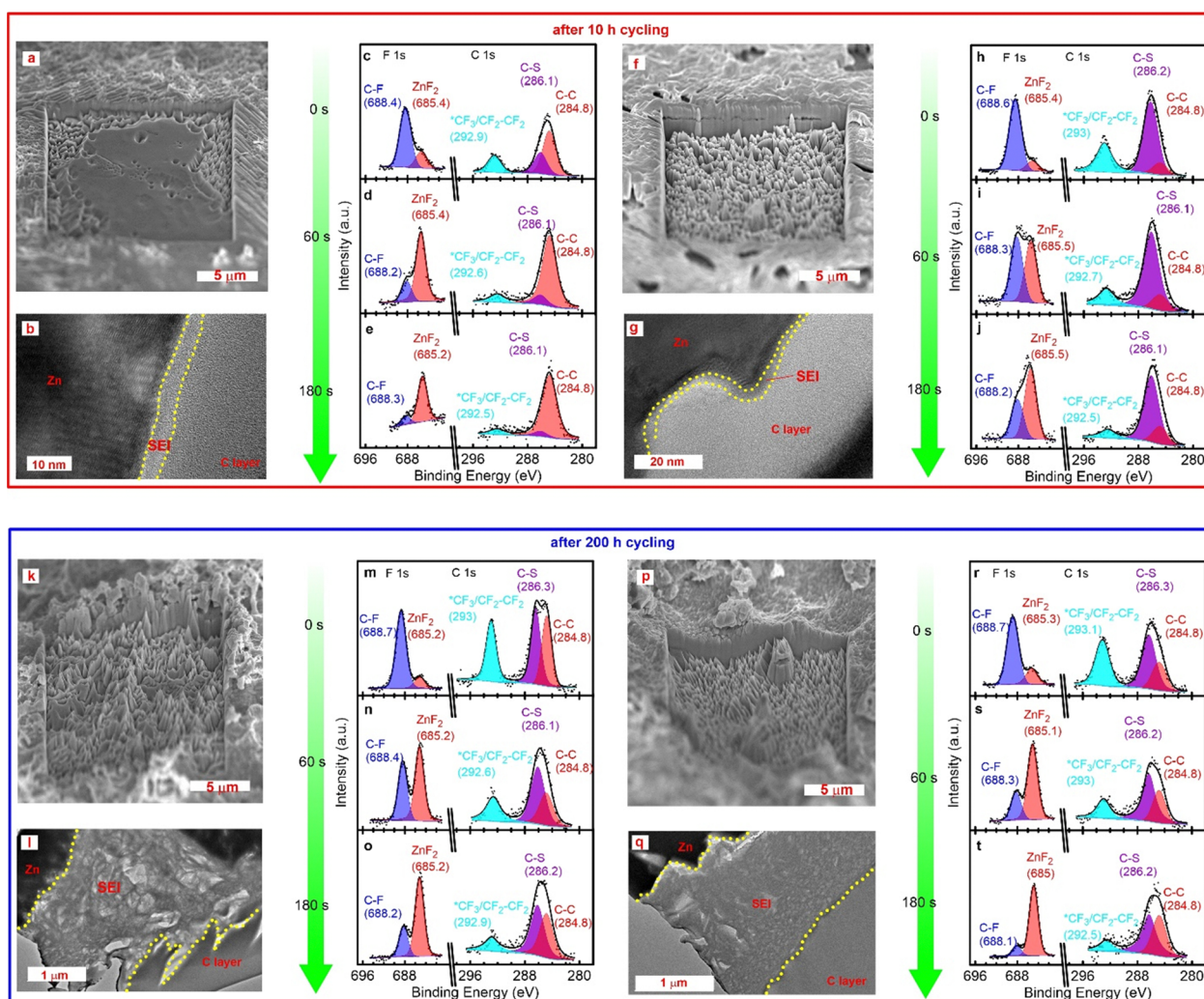


Fig. 2 Zn metal anode morphology and SEI evolution in aqueous electrolytes. (a)–(j), Zn metal anode morphology and SEI information after 10 h cycling (Zn|Zn cell setup, 0.5  $\text{mA cm}^{-2}$ , 0.5  $\text{mA h cm}^{-2}$  per cycle) at room temperature with different aqueous electrolytes: 1 m  $\text{Zn}(\text{TFSI})_2$  + 0.05 m TFMP in  $\text{H}_2\text{O}$  (a)–(e); 1 m  $\text{Zn}(\text{TFSI})_2$  + 1 m TEP + 0.05 m TFMP in  $\text{H}_2\text{O}$  (f)–(j). (k)–(t), Zn metal anode morphology and SEI information after 200 h cycling (Zn|Zn cell setup, 0.5  $\text{mA cm}^{-2}$ , 0.5  $\text{mA h cm}^{-2}$  per cycle) at room temperature with different aqueous electrolytes: 1 m  $\text{Zn}(\text{TFSI})_2$  + 0.05 m TFMP in  $\text{H}_2\text{O}$  (k)–(o); 1 m  $\text{Zn}(\text{TFSI})_2$  + 1 m TEP + 0.05 m TFMP in  $\text{H}_2\text{O}$  (p)–(t). Zn morphology was obtained using FIB-SEM (a), (f), (k), (p). SEI information was obtained using depth profile XPS (c)–(e), (h)–(j), (m)–(o), (r)–(t) and TEM (b), (g), (l), (q).



nano-ZnO clusters (Fig. S11, ESI<sup>†</sup>), a common component on Zn electrodes. From a kinetic perspective, this process could also be accelerated due to the increased Zn surface area as discussed above. Exposure to the X-ray beam could also contribute to Zn(TFSI)<sub>2</sub> salt composition.<sup>33</sup> As for the Zn electrodes cycled in 1 m Zn(TFSI)<sub>2</sub> + 0.05 m TFMP or 1 m Zn(TFSI)<sub>2</sub> + 1 m TEP + 0.05 m TFMP aqueous electrolytes, lingering C–F species (~688.5 eV) in F1s spectra and a ~293 eV peak in C1s spectra (Fig. 2(c)–(e), (h)–(j) and Fig. S10, ESI<sup>†</sup>) after 180 s of Ar<sup>+</sup> sputtering suggests the formation of TFMP-related interphasial species, which could be the main reason for improved Zn reversibility and will be discussed in detail in the next section. Note that the peak assignment for –CF<sub>3</sub> (~293 eV) and C–S (~286 eV), due to residual TFSI<sup>–</sup> anions or its decomposed products, follows previous reports.<sup>12,34</sup> A closer examination of the interphase using TEM shows a ~5 nm SEI layer on the Zn metal surface for TFMP aqueous samples (Fig. 2(b) and (g)), which is also complemented by the F signal in energy-dispersive X-ray spectroscopy (EDX, Fig. S12 and S13, ESI<sup>†</sup>).

After cycling for 200 h, Zn cycled in TFMP-containing electrolytes maintains a homogeneous morphology without dendrite formation (Fig. 2(k) and (p)). By observing C–F species (~688.5 eV) in the F1s spectra and a ~293 eV peak in the C1s spectra (Fig. 2(m)–(o) and (r)–(t)), the XPS depth profile confirms the remains of SEI chemistries due to TFMP-related reactions even after long-term cycling. Echoing recent reports on implausibly-thick SEI formation in aqueous Zn electrolytes,<sup>35,36</sup> the

evolution of SEI up to > 1 μm in these aqueous electrolytes was observed after 200 h cycling using TEM (Fig. 2(l) and (q)) with EDX confirmation (Fig. S14 and S15, ESI<sup>†</sup>). This is exceptional, especially compared to typical SEI growth on graphite or Li metal anodes in Li-based batteries.<sup>37,38</sup> This suggests that chemical reactions between the aqueous media and Zn electrode could facilitate the growth of thick and permeable interphase regions during long-term cycling; though, the mechanism(s) of Zn-ion conduction in such a thick SEI merits more thorough investigation.

Additionally, the participation of TFMP in the formation of SEI is indicated by the presence of a strong F signal during ToF-SIMS analysis on Zn electrodes obtained from aqueous and non-aqueous electrolytes based on Zn salts with F-free anions (Fig. S16, ESI<sup>†</sup>). To explore this mechanism, supporting DFT calculations were used to identify potential reaction pathways by which TFMP contributes to Zn interphasial chemistries and is accompanied with experimental results. First, DFT calculations were used to predict the relative binding free energies of different solvates (Fig. 3(a) and Fig. S17, ESI<sup>†</sup>). While TEP is found to easily displace water from the Zn solvation sheath (Fig. S17 and S18, ESI<sup>†</sup>) consistent with prior reports,<sup>26</sup> TFMP is not predicted to do so. However, TFMP is predicted to deprotonate on contact with ZnO, OH<sup>–</sup> or [Zn(OH)<sub>4</sub>]<sup>2–</sup> (Fig. S19, ESI<sup>†</sup>). The deprotonated species is an anion (TFMP<sub>H</sub>)<sup>–</sup> and is predicted to be able to displace water from the Zn solvation sheath and has stronger binding than even TEP (Fig. 3(c)). The 2-electron transfer to neutral Zn(H<sub>2</sub>O)<sub>4</sub>(TFMP<sub>H</sub>)<sub>2</sub> clusters yields

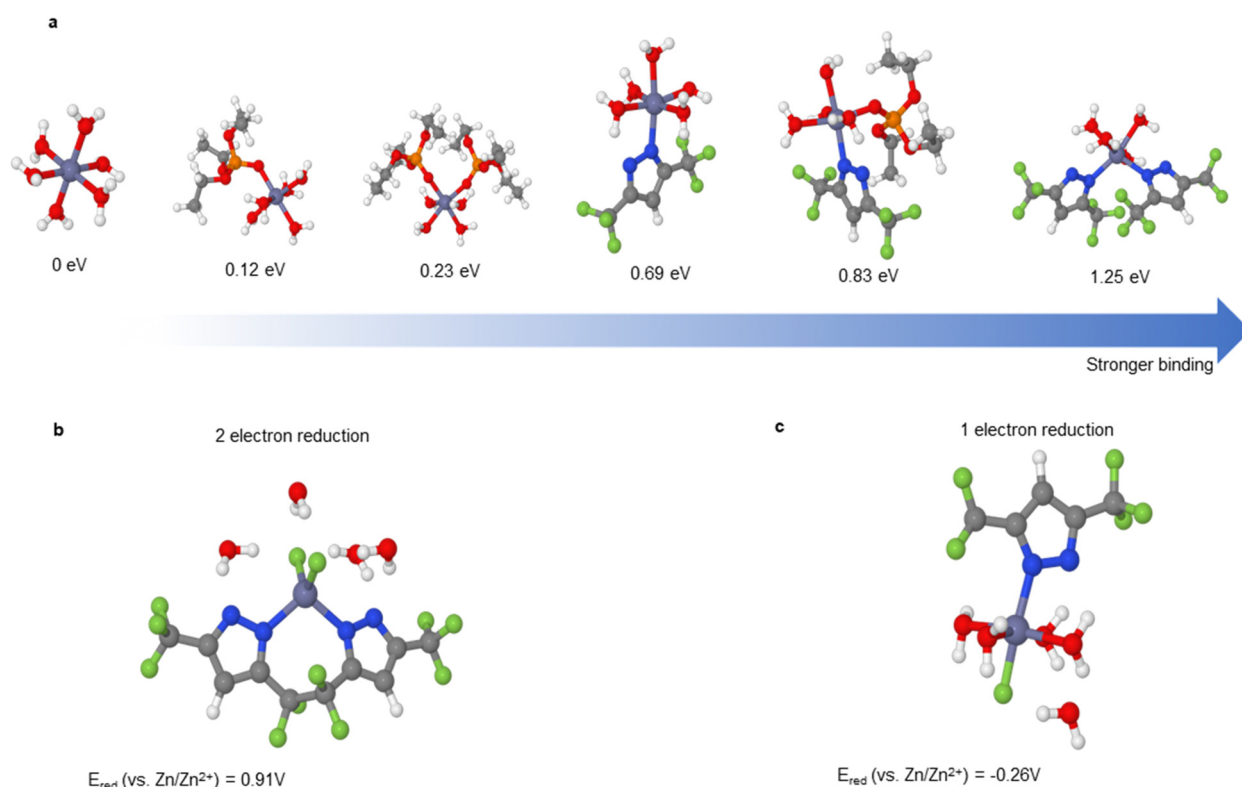


Fig. 3 Proposed SEI formation mechanisms for TFMP. (a), Binding free energies from DFT calculations relative to Zn(H<sub>2</sub>O)<sub>6</sub> in eV for various solvates comprising Zn, H<sub>2</sub>O, TEP, and TFMP<sub>H</sub>; the latter of which is an anion in these solvates. Higher values mean stronger binding. (b) and (c), DFT computed double (d) and single (e) electron reduction potentials of Zn solvates with two or one TFMP<sub>H</sub> anions.

a value of 0.91 V (vs.  $\text{Zn}^{2+}/\text{Zn}$ , Fig. 3(b)) in which each TFMP-<sub>H</sub> defluorinates and the resulting species dimerize across the terminal  $\text{CF}_2$  bonds. The products of this reduction exclude water and are likely an initial source of SEI formation at least from a thermodynamic perspective. By contrast, the solvate species produced by 1-electron reduction of  $\text{Zn}(\text{H}_2\text{O})_5(\text{TFMP-}_H)$  (Fig. 3(c)) is less likely to contribute to SEI formation with a reduction potential of  $-0.26$  V (Fig. 3(c)). Therefore, the impressive Zn anode reversibility (Fig. 1) is the combination of TEP suppressing dendrites and eliminating soft-shorts<sup>23,39</sup> while TFMP reacts and contributes to SEI formation. It's worth noting, TFMP becomes less effective in a basic environment compared to the mildly acidic environment (Fig. S3 and S4, ESI†), which could be due to formation of  $\text{K}(\text{TFMP-}_H)$  with KOH in the bulk instead of reacting locally at the zinc anode surface. To further enhance the reversibility of zinc anodes in more alkaline media, it is encouraged to explore

other entrainers that synergize and strengthen the formation of the robust SEI.

Similar postmortem analysis was applied to Zn metal anodes obtained from AN-based non-aqueous electrolytes. Differing from aqueous samples, the Zn morphology grown in the AN remains flat throughout the cycling protocol (Fig. 4(a) and (f)). In the C1s spectra of the control (Fig. 4(c)–(e)) and TFMP-derived samples (Fig. 4(h)–(j)), a peak at  $\sim 289.5$  eV can be detected at the very beginning stages of  $\text{Ar}^+$  bombardment, which suggests the presence of a thin, natural layer of carbonaceous species on the Zn surface. Except for this peak, no other peaks can be detected in both C1s and F1s spectra, even after sputtering for 180 s (Fig. 4(h)–(j)), which rules out the possibility of  $\text{TFSI}^-$  anion decomposition and is consistent with previous reports.<sup>31,40</sup> With the addition of 0.05 m TFMP,  $\text{ZnF}_2$  and C–F signals are detected in F1s spectra after only 10 h of cycling (Fig. 4(h)–(j)). Correspondingly, a peak at  $\sim 293$  eV is

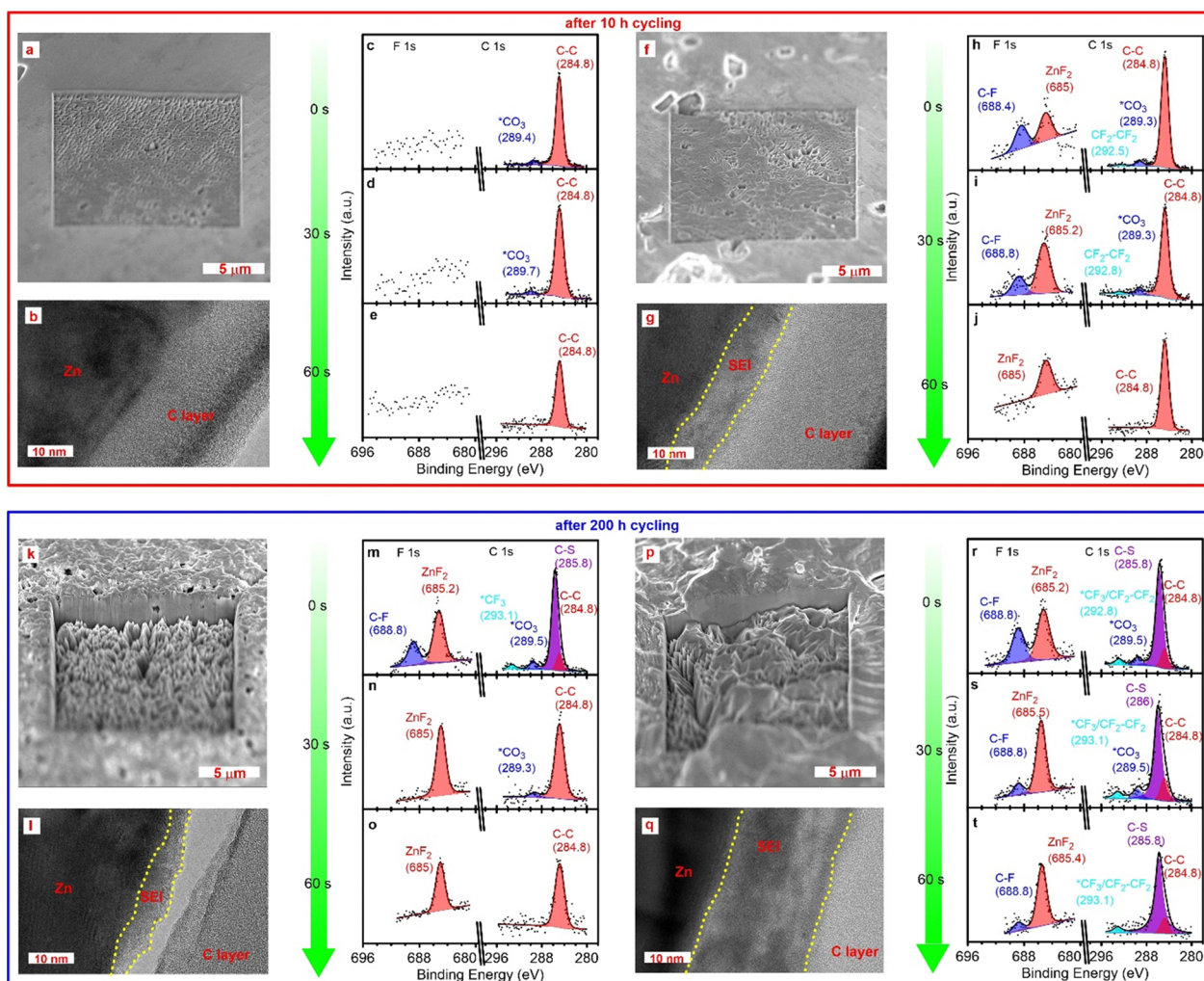


Fig. 4 Zn metal anode morphology and SEI evolution in non-aqueous electrolytes after different periods of cycling including both the 10 h and 200 h cycles. (a)–(j), Zn metal anode morphology and SEI information after 10 h cycling ( $\text{Zn}|\text{Zn}$  cell setup,  $0.5 \text{ mA cm}^{-2}$ ,  $0.5 \text{ mA h cm}^{-2}$  per cycle) at room temperature with different non-aqueous electrolytes:  $0.5 \text{ m Zn}(\text{TFSI})_2$  in AN (a)–(e);  $0.5 \text{ m Zn}(\text{TFSI})_2 + 0.05 \text{ m TFMP}$  in AN (f)–(j). (k)–(t), Zn metal anode morphology and SEI information after 200 h cycling ( $\text{Zn}|\text{Zn}$  cell setup,  $0.5 \text{ mA cm}^{-2}$ ,  $0.5 \text{ mA h cm}^{-2}$  per cycle) at room temperature with different non-aqueous electrolytes:  $0.5 \text{ m Zn}(\text{TFSI})_2$  in AN (k)–(o);  $0.5 \text{ m Zn}(\text{TFSI})_2 + 0.05 \text{ m TFMP}$  in AN (p)–(t). Zn morphology was obtained using FIB-SEM (a), (f), (k), (p). SEI information was obtained using depth profile XPS (c)–(e), (h)–(j), (m)–(o), (r)–(t) and TEM (b), (g), (l), (q).

shown in the C1s spectra (Fig. 4(h)–(j)), which should be assigned to  $(-\text{CF}_2-\text{CF}_2-)$  groups according to DFT calculations (Fig. 3) and was verified by observation of a  $\sim 10$  nm SEI layer under TEM (Fig. 4(g) and Fig. S20, ESI†). No such layer is observed on the AN control samples (Fig. 4(b)).

The Zn morphology in the AN-based electrolytes (Fig. 4(k) and (p)) changed dramatically, becoming very rough with increased surface area after cycling for 200 h. Surprisingly, the AN control electrolyte produces a  $\text{ZnF}_2$  peak in the F1s spectra even after sputtering (Fig. 4(m)–(o)). This likely indicates the decomposition of  $\text{TFSI}^-$  anions, due to electrochemically active regions of nano- $\text{ZnO}$ , as mentioned previously. The addition of TFMP increases the abundance of C–F species observed in the F1s spectra after sputtering (Fig. 4(r)–(t)), which further supports the existence of polymeric species (Fig. 3) contributing to the underlying SEI. In sharp contrast to the SEI evolution in aqueous media (Fig. 2(l) and (q)), the SEI thickness ( $< 20$  nm) does not grow substantially in the

non-aqueous electrolytes (Fig. 4(l) (q) and Fig. S21, ESI†) during 200 h of cycling.

## Full cell demonstrations

The extraordinary performance of Zn metal in TFMP-based electrolytes suggests significant promise toward practical RZMBs. Pursuing this direction, we selected two transition metal-free organic cathode chemistries to demonstrate the effectiveness of TFMP in both aqueous and non-aqueous electrolytes. RZMBs with excess Zn (100  $\mu\text{m}$  thickness) were prepared for screening purposes while thin (10  $\mu\text{m}$ ) and high areal capacity (5.85  $\text{mA h cm}^{-2}$ ) metal anodes were used in select cells as a rigorous demonstration aimed at commercial viability. PBQS exhibits a non-hydrated  $\text{Zn}^{2+}$ -ion storage linked to the quinone-related n-type redox reaction, while anions participate to a lesser extent in the reaction through

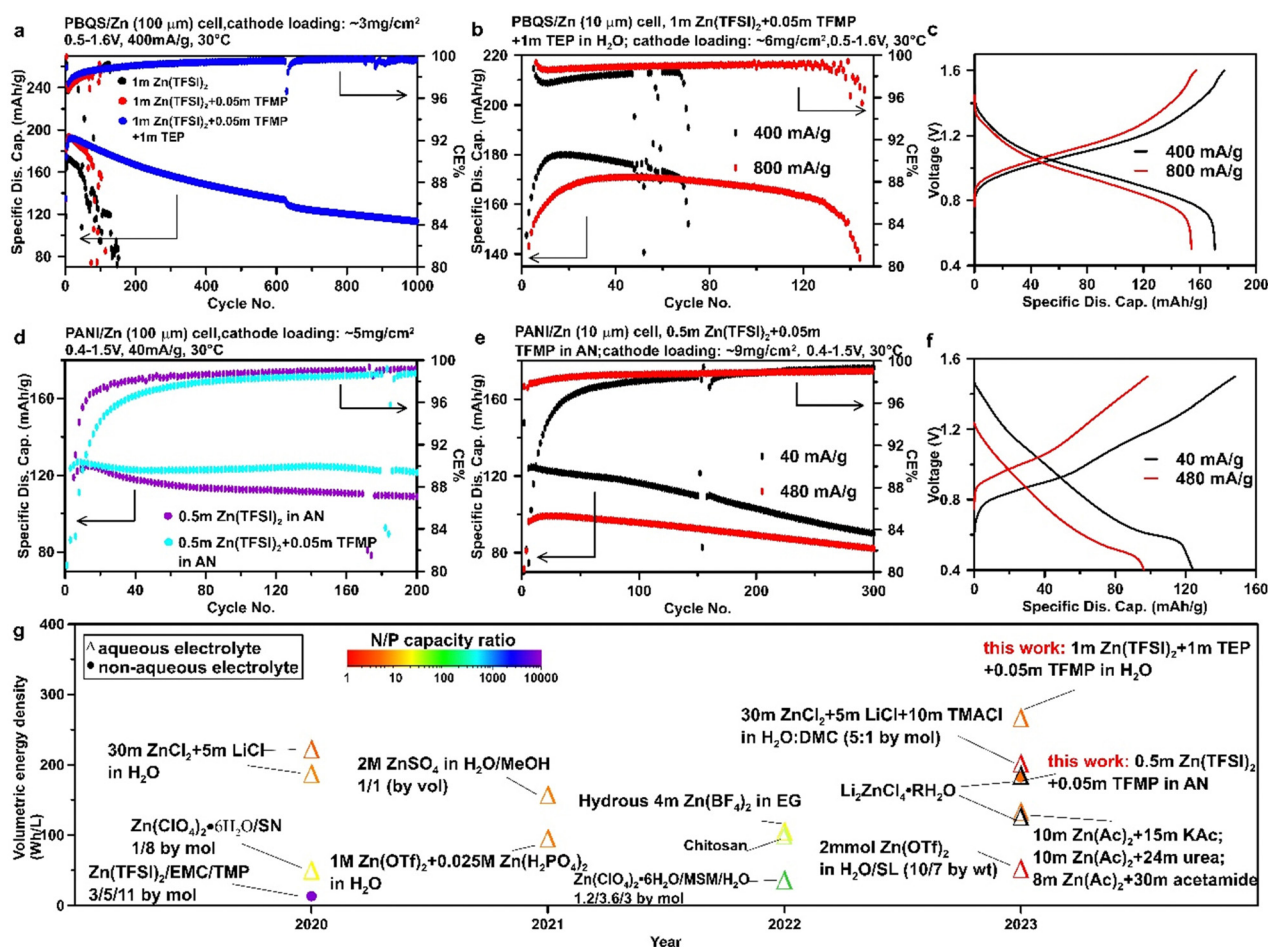


Fig. 5 Zn metal full battery performance. (a)–(c), PBQZn full battery performance (100- $\mu\text{m}$  Zn in (a) and 10- $\mu\text{m}$  Zn in (b) and (c)) for aqueous electrolytes with CE and corresponding specific discharge capacity vs. cycle number (a) and (b) and charge–discharge profile for 6th cycle after the system stabilizes following the initial activation cycles (c) between 0.5 and 1.6 V at 30 °C. (d) and (e), PANI|Zn full battery performance (100- $\mu\text{m}$  Zn in (d) and 10- $\mu\text{m}$  Zn in (e) and (f)) for AN-based non-aqueous electrolytes with CE and corresponding specific discharge capacity vs. cycle number (d), (e) and charge–discharge profile for 6th cycle after the system stabilizes following the initial activation cycles (f) between 0.4 and 1.5 V at 30 °C. (g) Cell-level volumetric energy density (only cathode and anode are counted) of selected full cell demonstration on Zn electrolyte efforts by publication year. Calculation was applied based on the 18 650-cylinder cell model proposed by Betz *et al.*<sup>54</sup> using the assumptions outlined in the experimental details.



p-dopable thioether linker.<sup>41,42</sup> Meanwhile, PANI predominately participates in the redox process *via* anion doping mechanism.<sup>43</sup> An initial capacity increase while cycling is observed in all the cases here due to the activation processes reported previously.<sup>43,44</sup> Compared to the control aqueous electrolyte of 1 m Zn(TFSI)<sub>2</sub>, the addition of 0.05 m TFMP alone shows moderate improvement of capacity retention. The 1 m Zn(TFSI)<sub>2</sub> + 0.05 m TFMP + 1 m TEP electrolyte demonstrates superior cycling stability in PBQS|Zn-excess cells with 80% of the maximum capacity retained even after 500 cycles (Fig. 5(a)). Upon optimization of the N/P ratio (the capacity ratio between negative and positive electrode) to 5.4, the aqueous 1 m Zn(TFSI)<sub>2</sub> + 0.05 m TFMP + 1 m TEP electrolyte in a PBQS|Zn-thin cells (PBQS: 6 mg cm<sup>-2</sup>, 1.08 mA h cm<sup>-2</sup> (estimated using 180 mA h g<sup>-1</sup>)/Zn (10 μm thickness, 7.14 mg cm<sup>-2</sup>, 5.85 mA h cm<sup>-2</sup>) exhibit > 80% retention of the maximum capacity after 70 and 130 cycles, respectively, with a high specific capacity at high rates (400 mA g<sup>-1</sup> and 800 mA g<sup>-1</sup>, corresponding to cathode active material mass) between 0.5 V and 1.6 V at 30 °C (Fig. 5(b) and (c)). A high Zn utilization per cycle of 20% and 16% (Fig. S22, ESI<sup>†</sup>), respectively, was also achieved during such testing at these rates which likely represent the most rigorous RZMB performance to date.

In non-aqueous electrolyte, the addition of 0.05 m TFMP results in better capacity retention after 200 cycles for PANI|Zn-excess cells (Fig. 5(d)), which could partially be attributed to the suppression of parasitic reactions on the Zn anode. The non-aqueous electrolyte also enables PANI|Zn-thin cells with an optimized N/P ratio of 5.4 (PANI: 9 mg cm<sup>-2</sup>, 1.08 mA h cm<sup>-2</sup> (estimated using 120 mA h g<sup>-1</sup>; Zn: 10 μm thickness, 7.14 mg cm<sup>-2</sup>, 5.85 mA h cm<sup>-2</sup>), at different rates (40 mA g<sup>-1</sup> and 480 mA g<sup>-1</sup>, Fig. 5(e) and (f)), and with >80% capacity retention after 300 cycles, corresponding to a Zn utilization per cycle of 19% and 15%, respectively (Fig. S22, ESI<sup>†</sup>).

To benchmark these results, we extracted the volumetric energy density from the most promising RZMBs described in the literature (Fig. S23 and S24, ESI<sup>†</sup>) with a complete discussion outlined in the experimental section and Table S1 (ESI<sup>†</sup>). By tuning the N/P ratio within our lab to ensure a high cell-level areal capacity and reasonably large fraction Zn utilization per cycle (~20%), this work demonstrates outstanding results among other aqueous and non-aqueous electrolyte efforts using organic cathode chemistries (Fig. 5(g)). Although some pioneering work has demonstrated practical N/P ratios (~1),<sup>25,45</sup> their volumetric energy density is limited due to the bottlenecks related to cathode materials (*i.e.* specific capacity and average voltage) and the electrode fabrication technique. To realize commercial RZMBs with compelling volumetric energy density, these challenges need to be addressed in parallel with electrolyte engineering.

## Conclusions

In this work, we demonstrated the utility of 3,5-bis(trifluoromethyl)pyrazole (TFMP) to form fluorinated polymeric interphase and significantly improve Zn reversibility in acidic, alkaline, and non-aqueous electrolytes. XPS depth profiling, TEM, and DFT

calculations confirmed the self-polymerization of TFMP as well as effects from the entrainer (*e.g.* TEP) which suppress dendritic Zn morphology and interfacial side reactions. Electrolytes based on this additive achieved high Zn plating/stripping CE (>99%) without dendrite growth, even for 10 μm thick Zn electrodes under aggressive testing conditions (in aqueous: 1.17 mA cm<sup>-2</sup>, 1.17 mA h cm<sup>-2</sup>, 20% Zn utilization per cycle; in non-aqueous: 9.36 mA cm<sup>-2</sup>, 4.68 mA h cm<sup>-2</sup>, 80% Zn utilization per cycle). Notably, Zn transport through the growing interphases observed in this work merits further exploration. Paired with various metal-free organic cathode electrodes, RZMBs with outstanding volumetric energy density were demonstrated in both aqueous (267 W h L<sup>-1</sup>) and non-aqueous electrolytes (182 W h L<sup>-1</sup>) while achieving ~20% Zn utilization per cycle. However, Zn cathodes with improved specific capacity, higher discharge voltages, and enhanced electronic conductivity are still urgently needed. This work reveals a new class of azole-based additives for engineering the interphasial chemistry in a wide spectrum of electrolyte compositions which holds tremendous potential for future RZMBs. The reversibility of other multivalent metal anodes could also benefit from the incorporation of TFMP, contingent on synchronized improvements in the transport kinetics of working ions.

## Methods

### Materials

Zinc trifluoromethanesulfonate (Zn(OTf)<sub>2</sub>, 98%), zinc chloride (ZnCl<sub>2</sub>, >98%) and zinc sulfate monohydrate (ZnSO<sub>4</sub>·H<sub>2</sub>O, 99.9%) were purchased from Sigma-Aldrich. Zinc bis(trifluoromethylsulfonyl)imide (Zn(TFSI)<sub>2</sub>, >99%), 3,5-bis(trifluoromethyl)pyrazole (TFMP, >98%) was purchased from Tokyo Chemical Industry. Acetonitrile (AN, 99.8%) and triethyl phosphate (TEP, >99.8%) were purchased from Sigma-Aldrich. These two solvents were dried using molecular sieves to ensure a low water content (<10 ppm) before electrolyte preparation. Zn foils with different thickness (10 μm (99.9%) and 100 μm (99.994%)) were purchased from Alfa Aesar.

All the electrolyte solutions were formulated by dissolving Zn salts and additives in de-ionized water (18 kΩ) or AN according to different concentrations in an Ar-filled glovebox. All the cathode electrode materials including poly(benzoquinonyl sulfide) (PBQS) and polyaniline (PANI) were synthesized according to previous reports.<sup>46,47</sup> The PBQS or PANI powders, Timical super C45 (MTI), and polytetrafluoroethylene (PTFE, Sigma-Aldrich) were dispersed in anhydrous 2-propanol (99.5%, Sigma-Aldrich) with a mass ratio of 7:2:1. The well-dispersed paste was then coated onto Ti mesh current collector, fully compressed with a rolling machine, and exposed at room temperature for 24 h to remove 2-propanol. The thickness of electrodes was measured using a micrometer (Mitutoyo).

### Characterizations

Infrared (IR) spectra were collected for aqueous electrolytes in an attenuated total internal reflection (ATR) geometry using a

Nicolet 6700 spectrometer (Thermo Scientific) with a diamond ATR setup. The spectra were the average of 64 scans collected at a resolution of  $2\text{ cm}^{-1}$ . The morphology of Zn metal electrodes obtained from Zn|Zn symmetric cells at zero state of charge after cycling with different current densities and areal capacities was studied using a scanning electron microscope (SEM, Hitachi SU-70). X-ray photoelectron spectroscopy (XPS) measurements (PHI Versaprobe III) were conducted on Zn electrodes obtained from Zn|Zn symmetric cells at zero state of charge after cycling with different current densities and areal capacities. Zn electrodes were obtained from cells in an argon filled glovebox, rinsed with anhydrous AN and dried in an antechamber under vacuum overnight, then transferred into XPS system by a sealed vacuum transfer setup. The XPS data was collected by using a combination of survey scan (pass energy  $224\text{ eV}$ , step size  $0.4\text{ eV}$ ) and high-resolution scan (pass energy  $55\text{ eV}$ , step size  $0.05\text{ eV}$ ) during  $\text{Ar}^+$  sputtering treatment. The X-ray with a power of  $25\text{ W}$  was focused to a spot size of  $100\text{ }\mu\text{m}$ . A combination of a low energy  $\text{Ar}$ -ion flow and an electron neutralizer was used for surface neutralization purpose. Sputtering  $\text{Ar}^+$  beam was set as  $500\text{ V}$  within a  $3\text{ mm} \times 3\text{ mm}$  region. XPS spectra peak was fitted with 70/30 Gaussian/Lorentzian line shapes on a Shirley background through PHI's Multipak software v. 9.6. All the XPS spectra were shifted relative to the binding energy of  $284.8\text{ eV}$  ( $\text{C1s sp}^3$ ) to compensate for any surface charging off-set during the measurement. The interphasial morphology and chemistry of Zn electrodes was characterized by a transmission electron microscopy (TEM, JOEL 2100F) with energy-dispersive X-ray spectroscopy (EDX) using Zn electrodes obtained from Zn|Zn symmetric cells at zero state of charge after cycling with different current densities and areal capacities. All the TEM samples were prepared by focused ion beam (FIB, Tescan GAIA). Prior to FIB preparation, a  $\sim 100\text{ nm}$  carbon layer and a tungsten-containing layer were also coated on the sample surface to protect the intact interphase. The distribution of fluorine at different depths in the cycled Zn electrodes was analyzed using time-of-flight secondary ion mass spectroscopy (ToF-SIMS) attached to a  $\text{Ga}^+$  based FIB-SEM (Tescan GAIA3) at an accelerated voltage of  $30\text{ kV}$  and  $1\text{ nA}$  current.

### Electrochemical measurements

The Cu|Zn, Zn|Zn, PBQS|Zn and PANI|Zn cells were examined in 2032-type coin cells consisting of glass fiber (Whatman GF/F) as separator and electrolytes ( $150\text{ }\mu\text{L}$  per cell). All the cells were prepared in an  $\text{Ar}$ -filled glovebox and tested using a Maccor charge-discharge unit. Zn plating/stripping coulombic efficiency (CE) was tested with two types of cell set-up: Cu|Zn ( $100\text{ }\mu\text{m}$ ) and Cu|Zn ( $10\text{ }\mu\text{m}$ ) at room temperature. For the initial screening purpose, Cu|Zn ( $100\text{ }\mu\text{m}$ ) cells were conducted following the protocol proposed by previous report.<sup>26</sup> Cu electrode was conditioned by plating ( $0.5\text{ mA cm}^{-2}$ ,  $5\text{ mA h cm}^{-2}$ ) and stripping Zn ( $0.5\text{ V}$ ) firstly. Then a Zn reservoir with a capacity of  $5\text{ mA h cm}^{-2}$  ( $Q_i$ ) was deposited on Cu by using  $0.5\text{ mA cm}^{-2}$  during the following cycle. Afterwards, Zn was plated and stripped during the following 9 cycles with

$0.5\text{ mA cm}^{-2}$ ,  $1\text{ mA h cm}^{-2}$  ( $Q_c$ ) in each cycle. A capacity ( $Q_s$ ) was detected when plated Zn was stripped by charging to  $0.5\text{ V}$  in the final step. The average CE is obtained based on eqn 1:

$$\text{CE} = \frac{9Q_c + Q_s}{9Q_c + Q_i} \quad (1)$$

For the purpose of practical application, Cu|Zn ( $10\text{ }\mu\text{m}$ ) cell setup was used for further CE measurement. During each cycle, Zn was plated on Cu electrode by discharging the cell using two conditions:  $1.17\text{ mA cm}^{-2}$ ,  $1.17\text{ mA h cm}^{-2}$  ( $Q_p$ , 20% Zn utilization per cycle) or  $9.36\text{ mA cm}^{-2}$ ,  $4.68\text{ mA h cm}^{-2}$  ( $Q_p$ , 80% Zn utilization per cycle), then Zn was stripped by charging the cell to  $0.5\text{ V}$  ( $Q_s$ ). CE for each cycle is calculated based on eqn (2):

$$\text{CE} = \frac{Q_s}{Q_p} \quad (2)$$

Zn|Zn ( $100\text{ }\mu\text{m}$ ) symmetric cell setup was tested using different current densities ( $0.5$ ,  $1$  or  $2.5\text{ mA cm}^{-2}$ ) at room temperature. Each charge/discharge step was set as 1 hour. The leverage of aqueous electrolyte in full cell was applied by using two types of cell set-up: PBQS ( $\sim 3\text{ mg cm}^{-2}$ )|Zn ( $100\text{ }\mu\text{m}$ ) and PBQS ( $\sim 6\text{ mg cm}^{-2}$ )|Zn ( $10\text{ }\mu\text{m}$ ) at  $30\text{ }^\circ\text{C}$  between  $0.5\text{ V}$  and  $1.6\text{ V}$  with  $400\text{ mA g}^{-1}$  and  $800\text{ mA g}^{-1}$  (based on PBQS mass), respectively. The leverage of non-aqueous electrolyte in full cell was applied by using another two types of cell set-up: PANI ( $\sim 5\text{ mg cm}^{-2}$ )|Zn ( $100\text{ }\mu\text{m}$ ) and PANI ( $\sim 9\text{ mg cm}^{-2}$ )|Zn ( $10\text{ }\mu\text{m}$ ) at  $30\text{ }^\circ\text{C}$  between  $0.4\text{ V}$  and  $1.5\text{ V}$  with  $40\text{ mA g}^{-1}$  and  $480\text{ mA g}^{-1}$  (based on PANI mass), respectively. Electrochemical impedance spectroscopy (EIS) measurements were conducted on Zn|Zn symmetric cells with selected electrolytes before or after 10 h and 200 h cycling at zero state of charge at  $25\text{ }^\circ\text{C}$  ( $0.5\text{ mA cm}^{-2}$ ,  $0.5\text{ mA h cm}^{-2}$ ). All the spectra were collected with ten points per decade from  $100\text{ kHz}$  to  $10\text{ mHz}$  with a signal amplitude of  $10\text{ mV}$  at  $25\text{ }^\circ\text{C}$  by using a single-channel Gamry Potentiostat (Reference 3000). Electrochemical stability window measurements were conducted with a three electrode Swagelok cell containing stainless steel (SS) as the working electrode, carbon black as the counter electrode and  $\text{Ag/AgCl}$  as the reference electrode. The measurements were carried out using a single channel Gamry Potentiostat (Reference 3000) with a scan rate of  $5\text{ mV s}^{-1}$  at room temperature within different voltage ranges:  $-1\text{ V}$  to  $0\text{ V}$  for cathodic region;  $0\text{ V}$  to  $2\text{ V}$  for anodic region.

## Computational methods

### General

Unless otherwise mentioned, all density functional theory calculations are performed with Gaussian16 rev. C.02 while input files are created using the atomic simulation environment (ASE).<sup>48,49</sup>

### Binding free energies

Many variations of clusters with compositions:  $\text{Zn}[(\text{H}_2\text{O})_x\text{TEPy}(\text{TFMP})_z]$  and  $\text{Zn}[(\text{H}_2\text{O})_x\text{TEPy}(\text{TFMP-H})_z]$  where  $x = (4, 5, 6)$ ,

$y = (0, 1, 2)$ , and  $z = (0, 1, 2)$  given the constraint that  $x + y + z = 6$ , were prepared using the NCI ensemble method in CREST. TFMP-H is the anion of TFMP with the N-H proton removed. Conformer sampling was also performed for the individual molecules as well using a combination of the conformer sampling tools in CREST as well as an in-house script using RDKit.<sup>50</sup> For the cases with multiple TEP, TFMP, or a mix of 1 TEP and 1 TFMP, we explicitly consider cluster generation starting from these molecules placed in the axial and neighboring equatorial positions. The geometries of over 120 different octahedral clusters are optimized at the PCM(acetone)/M05-2X/6-31+G(d,p) level of theory. Binding free energies are computed as,

$$\Delta G_b = G_{\text{XS}}^{\text{XS}} - G_{\text{X}}^{\circ, \text{X}} - \sum G_{\text{s}}^{\text{s}}$$

where,  $\Delta G_b$  is the binding free energy,  $G_{\text{XS}}^{\text{XS}}$  is the free energy of the cluster immersed in implicit solvent,  $G_{\text{X}}^{\circ, \text{X}}$  is the gas phase free energy of the  $\text{Zn}^{2+}$  ion, and  $\sum G_{\text{s}}^{\text{s}}$  is the sum of free energies of the different solvating species immersed in implicit solvent.  $G_{\text{s}}^{\text{s}}$  reflects the free energy of isolated TEP, TFMP, or TFMP-H but the average free energy per water from a  $(\text{H}_2\text{O})_6$  cluster. The resulting binding free energies more closely resemble the solvation free energy of  $\text{Zn}^{2+}$  as a result.<sup>51</sup>

### Reduction potentials

Reduction potentials of TFMP-H containing solvates were computed using the Nernst equation for 1 or 2-electron reductions as,

$$E^{\text{red}} = -\frac{G(A^-) - G(A)}{nF} - 3.68 \text{ V}$$

where,  $n$  is the number of electrons in the reduction,  $F$  is Faraday's constant,  $G(A^-)$  is the free energy of the reduced species, and  $G(A)$  is the same free energy used in  $G_{\text{XS}}^{\text{XS}}$  for the species with the largest binding free energy (most negative). The clusters of reduced species were generated by a combination of manual editing using software like Avogadro and automated ensemble generation starting from the hand-edited structure.<sup>52</sup> Single and doubly defluorinated species are considered along with dimerization of the terminal  $\text{CF}_2$  groups of adjacent TFMP-H species if appropriate. A value of 3.68 V is used to shift the voltage to the  $\text{Zn}^{2+}/\text{Zn}$  scale using a value of 4.44 V for the absolute value of the standard hydrogen electrode and  $-0.76$  V for the standard reduction potential of  $\text{Zn}^{2+}/\text{Zn}$ . There is no consensus on the exact value of the absolute standard hydrogen electrode potential and it may drift depending on the electrolyte composition. The value of this conversion may be subject to change in the future but is the best we can do today. Any references or comparisons to TFSI<sup>-</sup> decomposition outside what is shown here are taken from our previous work.<sup>30</sup>

### TFMP/TFSI reactivity on ZnO particle

The  $(\text{ZnO})_{12}$  nanoparticle was adapted from previous work.<sup>53</sup> As with the other calculations, CREST/xTB was used to sample different adsorption sites and orientations of the TFMP/TFSI,

or  $\text{Zn}^{2+}$ -TFMP. The ZnO nanoparticle was fixed for these calculations. All calculations were performed at the PCM(acetone)/M05-2X/6-31+G(d,p) level of theory. The reduction potential is computed as above while the reaction energy is just the difference in free energies between the product and reactant states.

## Conflicts of interest

This work has been filed as US Patent application no. 20230223595A1.

## Acknowledgements

This work was supported by the Joint Center for Energy Storage Research (JCESR), an Energy Innovation Hub funded by Department of Energy, through IAA SN2020957. Dr Lin Ma at UNC Charlotte acknowledges the support from the Dr Brad. E. Forch Distinguished Postdoctoral Fellowship and the support by the US National Science Foundation award no. 2301719. The authors thanks Dr Jiancun Rao and Dr Sz-Chian Liou (UMD AIM-Lab) for TEM assistance. Dr Chao Luo acknowledges the support from the George Mason University Quantum Science & Engineering Center. Drs. L. M., T. P., M. S., G. P., and O. B. wish to acknowledge the many years of service and leadership of Dr Kang Xu who has retired from federal service.

## References

- 1 A. Elshkaki, B. K. Reck and T. E. Graedel, Anthropogenic nickel supply, demand, and associated energy and water use, *Resour., Conserv. Recycl.*, 2017, **125**, 300–307, DOI: [10.1016/j.resconrec.2017.07.002](https://doi.org/10.1016/j.resconrec.2017.07.002).
- 2 G. A. Campbell, The cobalt market revisited, *Miner. Econ.*, 2020, **33**, 21–28, DOI: [10.1007/s13563-019-00173-8](https://doi.org/10.1007/s13563-019-00173-8).
- 3 C. B. Tabelin, *et al.*, Towards a low-carbon society: A review of lithium resource availability, challenges and innovations in mining, extraction and recycling, and future perspectives, *Miner. Eng.*, 2021, **163**, 106743, DOI: [10.1016/j.mineng.2020.106743](https://doi.org/10.1016/j.mineng.2020.106743).
- 4 M. Winter, B. Barnett and K. Xu, Before Li Ion Batteries, *Chem. Rev.*, 2018, **118**, 11433–11456, DOI: [10.1021/acs.chemrev.8b00422](https://doi.org/10.1021/acs.chemrev.8b00422).
- 5 J. F. Parker, *et al.*, Rechargeable nickel–3D zinc batteries: An energy-dense, safer alternative to lithium-ion, *Science*, 2017, **356**, 415–418, DOI: [10.1126/science.aak9991](https://doi.org/10.1126/science.aak9991).
- 6 A. A. Yaroshevsky, Abundances of chemical elements in the Earth's crust, *Geochem. Int.*, 2006, **44**, 48–55, DOI: [10.1134/S001670290601006X](https://doi.org/10.1134/S001670290601006X).
- 7 Q. Yang, *et al.*, Dendrites in Zn-Based Batteries, *Adv. Mater.*, 2020, **32**, 2001854, DOI: [10.1002/adma.202001854](https://doi.org/10.1002/adma.202001854).
- 8 L. E. Blanc, D. Kundu and L. F. Nazar, Scientific Challenges for the Implementation of Zn-Ion Batteries, *Joule*, 2020, **4**, 771–799, DOI: [10.1016/j.joule.2020.03.002](https://doi.org/10.1016/j.joule.2020.03.002).
- 9 M. A. Schroeder, L. Ma, G. Pastel and K. Xu, The mystery and promise of multivalent metal-ion batteries, *Curr. Opin.*



- Electrochem.*, 2021, **29**, 100819, DOI: [10.1016/j.coelec.2021.100819](https://doi.org/10.1016/j.coelec.2021.100819).
- 10 J. Han, *et al.*, A Thin and Uniform Fluoride-Based Artificial Interphase for the Zinc Metal Anode Enabling Reversible Zn/MnO<sub>2</sub> Batteries, *ACS Energy Lett.*, 2021, **6**, 3063–3071, DOI: [10.1021/acsenergylett.1c01249](https://doi.org/10.1021/acsenergylett.1c01249).
  - 11 Y. Li, *et al.*, A stable fluoride-based interphase for a long cycle Zn metal anode in an aqueous zinc ion battery, *J. Mater. Chem. A*, 2022, **10**, 14399–14410, DOI: [10.1039/D2TA03550B](https://doi.org/10.1039/D2TA03550B).
  - 12 L. Ma, *et al.*, Functionalized Phosphonium Cations Enable Zinc Metal Reversibility in Aqueous Electrolytes, *Angew. Chem., Int. Ed.*, 2021, **60**, 12438–12445, DOI: [10.1002/anie.202017020](https://doi.org/10.1002/anie.202017020).
  - 13 A. Bayaguud, X. Luo, Y. Fu and C. Zhu, Cationic Surfactant-Type Electrolyte Additive Enables Three-Dimensional Dendrite-Free Zinc Anode for Stable Zinc-Ion Batteries, *ACS Energy Lett.*, 2020, **5**, 3012–3020, DOI: [10.1021/acsenergylett.0c01792](https://doi.org/10.1021/acsenergylett.0c01792).
  - 14 W. Yang, *et al.*, Hydrated Eutectic Electrolytes with Ligand-Oriented Solvation Shells for Long-Cycling Zinc-Organic Batteries, *Joule*, 2020, **4**, 1557–1574, DOI: [10.1016/j.joule.2020.05.018](https://doi.org/10.1016/j.joule.2020.05.018).
  - 15 C. Zhang, *et al.*, A ZnCl<sub>2</sub> water-in-salt electrolyte for a reversible Zn metal anode, *Chem. Commun.*, 2018, **54**, 14097–14099, DOI: [10.1039/C8CC07730D](https://doi.org/10.1039/C8CC07730D).
  - 16 D. Zhang, *et al.*, Electrodeposition of Zinc in Aqueous Electrolytes Containing High Molecular Weight Polymers, *Macromolecules*, 2020, **53**, 2694–2701, DOI: [10.1021/acs.macromol.0c00037](https://doi.org/10.1021/acs.macromol.0c00037).
  - 17 T. Li, *et al.*, Engineering Fluorine-rich Double Protective Layer on Zn Anode for Highly Reversible Aqueous Zinc-ion Batteries, *Angew. Chem., Int. Ed.*, 2023, **62**, e202314883, DOI: [10.1002/anie.202314883](https://doi.org/10.1002/anie.202314883).
  - 18 H. Qiu, *et al.*, Zinc anode-compatible in-situ solid electrolyte interphase via cation solvation modulation, *Nat. Commun.*, 2019, **10**, 5374, DOI: [10.1038/s41467-019-13436-3](https://doi.org/10.1038/s41467-019-13436-3).
  - 19 M. Bayer, *et al.*, Influence of Water Content on the Surface Morphology of Zinc Deposited from EMImOTf/Water Mixtures, *J. Electrochem. Soc.*, 2019, **166**, A909–A914, DOI: [10.1149/2.0121906jes](https://doi.org/10.1149/2.0121906jes).
  - 20 L. Ma, *et al.*, Liquid-Free All-Solid-State Zinc Batteries and Encapsulation-Free Flexible Batteries Enabled by In Situ Constructed Polymer Electrolyte, *Angew. Chem., Int. Ed.*, 2020, **59**, 23836–23844, DOI: [10.1002/anie.202011788](https://doi.org/10.1002/anie.202011788).
  - 21 S. Zhao, *et al.*, Self-Healing and Anti-CO<sub>2</sub> Hydrogels for Flexible Solid-State Zinc-Air Batteries, *ACS Appl. Mater. Interfaces*, 2021, **13**, 12033–12041, DOI: [10.1021/acsami.1c00012](https://doi.org/10.1021/acsami.1c00012).
  - 22 A. Naveed, *et al.*, A Highly Reversible Zn Anode with Intrinsically Safe Organic Electrolyte for Long-Cycle-Life Batteries, *Adv. Mater.*, 2019, **31**, 1900668, DOI: [10.1002/adma.201900668](https://doi.org/10.1002/adma.201900668).
  - 23 A. Naveed, H. Yang, J. Yang, Y. Nuli and J. Wang, Highly Reversible and Rechargeable Safe Zn Batteries Based on a Triethyl Phosphate Electrolyte, *Angew. Chem., Int. Ed.*, 2019, **58**, 2760–2764, DOI: [10.1002/anie.201813223](https://doi.org/10.1002/anie.201813223).
  - 24 F. Wang, *et al.*, Highly reversible zinc metal anode for aqueous batteries, *Nat. Mater.*, 2018, **17**, 543–549, DOI: [10.1038/s41563-018-0063-z](https://doi.org/10.1038/s41563-018-0063-z).
  - 25 C. Li, *et al.*, Enabling selective zinc-ion intercalation by a eutectic electrolyte for practical anodeless zinc batteries, *Nat. Commun.*, 2023, **14**, 3067, DOI: [10.1038/s41467-023-38460-2](https://doi.org/10.1038/s41467-023-38460-2).
  - 26 L. Ma, *et al.*, Critical Factors Dictating Reversibility of the Zinc Metal Anode, *Energy Environ. Mater.*, 2020, **3**, 516–521, DOI: [10.1002/eeem2.12077](https://doi.org/10.1002/eeem2.12077).
  - 27 P. Albertus, S. Babinec, S. Litzelman and A. Newman, Status and challenges in enabling the lithium metal electrode for high-energy and low-cost rechargeable batteries, *Nat. Energy*, 2018, **3**, 16–21, DOI: [10.1038/s41560-017-0047-2](https://doi.org/10.1038/s41560-017-0047-2).
  - 28 L. Ma, *et al.*, Realizing high zinc reversibility in rechargeable batteries, *Nat. Energy*, 2020, **5**, 743–749, DOI: [10.1038/s41560-020-0674-x](https://doi.org/10.1038/s41560-020-0674-x).
  - 29 Q. Li, A. Chen, D. Wang, Z. Pei and C. Zhi, “Soft Shorts” Hidden in Zinc Metal Anode Research, *Joule*, 2022, **6**, 273–279, DOI: [10.1016/j.joule.2021.12.009](https://doi.org/10.1016/j.joule.2021.12.009).
  - 30 L. Ma, *et al.*, Ammonium enables reversible aqueous Zn battery chemistries by tailoring the interphase, *One Earth*, 2022, **5**, 413–421, DOI: [10.1016/j.oneear.2022.03.012](https://doi.org/10.1016/j.oneear.2022.03.012).
  - 31 L. Suo, *et al.*, “Water-in-salt” electrolyte enables high-voltage aqueous lithium-ion chemistries, *Science*, 2015, **350**, 938–943, DOI: [10.1126/science.aab1595](https://doi.org/10.1126/science.aab1595).
  - 32 N. Dubouis, *et al.*, The role of the hydrogen evolution reaction in the solid–electrolyte interphase formation mechanism for “Water-in-Salt” electrolytes, *Energy Environ. Sci.*, 2018, **11**, 3491–3499, DOI: [10.1039/C8EE02456A](https://doi.org/10.1039/C8EE02456A).
  - 33 H.-G. Steinrück, *et al.*, Interfacial Speciation Determines Interfacial Chemistry: X-ray-Induced Lithium Fluoride Formation from Water-in-salt Electrolytes on Solid Surfaces, *Angew. Chem., Int. Ed.*, 2020, **59**, 23180–23187, DOI: [10.1002/anie.202007745](https://doi.org/10.1002/anie.202007745).
  - 34 J. Alvarado, *et al.*, Bisalt ether electrolytes: a pathway towards lithium metal batteries with Ni-rich cathodes, *Energy Environ. Sci.*, 2019, **12**, 780–794, DOI: [10.1039/C8EE02601G](https://doi.org/10.1039/C8EE02601G).
  - 35 L. Cao, *et al.*, Fluorinated interphase enables reversible aqueous zinc battery chemistries, *Nat. Nanotechnol.*, 2021, **16**, 902–910, DOI: [10.1038/s41565-021-00905-4](https://doi.org/10.1038/s41565-021-00905-4).
  - 36 X. Zeng, *et al.*, Electrolyte Design for In Situ Construction of Highly Zn<sup>2+</sup>-Conductive Solid Electrolyte Interphase to Enable High-Performance Aqueous Zn-Ion Batteries under Practical Conditions, *Adv. Mater.*, 2021, **33**, 2007416, DOI: [10.1002/adma.202007416](https://doi.org/10.1002/adma.202007416).
  - 37 X. Cao, *et al.*, Monolithic solid–electrolyte interphases formed in fluorinated orthoformate-based electrolytes minimize Li depletion and pulverization, *Nat. Energy*, 2019, **4**, 796–805, DOI: [10.1038/s41560-019-0464-5](https://doi.org/10.1038/s41560-019-0464-5).
  - 38 M. Nie, *et al.*, Role of Solution Structure in Solid Electrolyte Interphase Formation on Graphite with LiPF<sub>6</sub> in Propylene Carbonate, *J. Phys. Chem. C*, 2013, **117**, 25381–25389, DOI: [10.1021/jp409765w](https://doi.org/10.1021/jp409765w).
  - 39 S. Liu, *et al.*, Tuning the Electrolyte Solvation Structure to Suppress Cathode Dissolution, Water Reactivity, and Zn

- Dendrite Growth in Zinc-Ion Batteries, *Adv. Funct. Mater.*, 2021, **31**, 2104281, DOI: [10.1002/adfm.202104281](https://doi.org/10.1002/adfm.202104281).
- 40 A. S. Etman, M. Carboni, J. Sun and R. Younesi, Acetonitrile-Based Electrolytes for Rechargeable Zinc Batteries, *Energy Technol.*, 2020, **8**, 2000358, DOI: [10.1002/ente.202000358](https://doi.org/10.1002/ente.202000358).
- 41 Y. Zhang, Y. Liang, H. Dong, X. Wang and Y. Yao, Charge Storage Mechanism of a Quinone Polymer Electrode for Zinc-ion Batteries, *J. Electrochem. Soc.*, 2020, **167**, 070558, DOI: [10.1149/1945-7111/ab847a](https://doi.org/10.1149/1945-7111/ab847a).
- 42 Y. Zhang, L. Zhao, Y. Liang, X. Wang and Y. Yao, Effect of electrolyte anions on the cycle life of a polymer electrode in aqueous batteries, *eScience*, 2022, **2**, 110–115, DOI: [10.1016/j.esci.2022.01.002](https://doi.org/10.1016/j.esci.2022.01.002).
- 43 H.-Y. Shi, Y.-J. Ye, K. Liu, Y. Song and X. Sun, A Long-Cycle-Life Self-Doped Polyaniline Cathode for Rechargeable Aqueous Zinc Batteries, *Angew. Chem., Int. Ed.*, 2018, **57**, 16359–16363, DOI: [10.1002/anie.201808886](https://doi.org/10.1002/anie.201808886).
- 44 T. Sun, *et al.*, Poly(2,5-Dihydroxy-1,4-Benzoquinonyl Sulfide) As an Efficient Cathode for High-Performance Aqueous Zinc–Organic Batteries, *Adv. Funct. Mater.*, 2021, **31**, 2010049, DOI: [10.1002/adfm.202010049](https://doi.org/10.1002/adfm.202010049).
- 45 H. Jiang, *et al.*, Chloride electrolyte enabled practical zinc metal battery with a near-unity Coulombic efficiency, *Nat. Sustain.*, 2023, **6**, 806–815, DOI: [10.1038/s41893-023-01092-x](https://doi.org/10.1038/s41893-023-01092-x).
- 46 Z. Song, Y. Qian, T. Zhang, M. Otani and H. Zhou, Poly-(benzoquinonyl sulfide) as a High-Energy Organic Cathode for Rechargeable Li and Na Batteries, *Adv. Sci.*, 2015, **2**, 1500124, DOI: [10.1002/advs.201500124](https://doi.org/10.1002/advs.201500124).
- 47 F. Wan, *et al.*, An Aqueous Rechargeable Zinc–Organic Battery with Hybrid Mechanism, *Adv. Funct. Mater.*, 2018, **28**, 1804975, DOI: [10.1002/adfm.201804975](https://doi.org/10.1002/adfm.201804975).
- 48 A. Hjorth Larsen, *et al.*, The atomic simulation environment—a Python library for working with atoms, *J. Phys.: Condens. Matter*, 2017, **29**, 273002, DOI: [10.1088/1361-648X/aa680e](https://doi.org/10.1088/1361-648X/aa680e).
- 49 *Gaussian 16 Rev. C.01*, Wallingford, C., 2016.
- 50 rdkit/rdkit: 2022\_09\_3 (Q3 2022) Release (Release\_2022\_09\_3. (Zenodo)).
- 51 D. Asthagiri, L. R. Pratt, M. E. Paulaitis and S. B. Rempe, Hydration Structure and Free Energy of Biomolecularly Specific Aqueous Dications, Including  $\text{Zn}^{2+}$  and First Transition Row Metals, *J. Am. Chem. Soc.*, 2004, **126**, 1285–1289, DOI: [10.1021/ja0382967](https://doi.org/10.1021/ja0382967).
- 52 M. D. Hanwell, *et al.*, Avogadro: an advanced semantic chemical editor, visualization, and analysis platform, *J. Cheminf.*, 2012, **4**, 17, DOI: [10.1186/1758-2946-4-17](https://doi.org/10.1186/1758-2946-4-17).
- 53 L. Ma, *et al.*, Highly reversible Zn metal anode enabled by sustainable hydroxyl chemistry, *Proc. Natl. Acad. Sci. U. S. A.*, 2022, **119**, e2121138119, DOI: [10.1073/pnas.2121138119](https://doi.org/10.1073/pnas.2121138119).
- 54 J. Betz, *et al.*, Theoretical versus Practical Energy: A Plea for More Transparency in the Energy Calculation of Different Rechargeable Battery Systems, *Adv. Energy Mater.*, 2019, **9**, 1803170, DOI: [10.1002/aenm.201803170](https://doi.org/10.1002/aenm.201803170).